ELSEVIER

Sensors and Actuators A 95 (2002) 212–221

SENSORS AND ACTUATORS A PHYSICAL

www.elsevier.com/locate/sna

Vertical comb-finger capacitive actuation and sensing for CMOS-MEMS

Huikai Xie[a,*], Gary K. Fedder[a,b]

[a]Department of Electrical and Computer Engineering, Carnegie Mellon University, Pittsburgh, PA 15213, USA
[b]The Robotics Institute, Carnegie Mellon University, Pittsburgh, PA 15213, USA

Abstract

A new method for out-of-plane (vertical) electrostatic actuation and capacitive displacement-sensing that utilizes sidewall capacitance change of multiconductor comb fingers is analyzed and experimentally verified. Combining the inherited in-plane (lateral) actuation and sensing capacities of comb fingers, three-dimensional actuation/sensing can be realized. A maskless post-CMOS micromachining process is employed and the fabrication is compatible with standard CMOS processes. Applications include an three-axis microstage, a *z*-axis accelerometer and a lateral-axis gyroscope that use the proposed vertical comb-finger actuation/sensing method. The measured maximum vertical displacement of the microstage is 3.5 μm with a resonant frequency of 6.17 kHz. Measured sensitivity of the *z*-axis accelerometer is 0.5 mV/g with less than −40 dB cross-axis sensitivity, noise floor 6 mg/$\sqrt{\text{Hz}}$, and linear range from −27 to 27 g. The lateral-axis gyroscope design uses integrated comb drives for out-of-plane actuation, and is motivated by the desire to integrate three-axis gyroscopes on a single chip. The packaged gyroscope operates at atmospheric pressure with a sensitivity of 0.12 mV/°/s and the resonant frequency of the drive mode is thermomechanically tuned between 4.2–5.1 kHz. Resonant frequency matching between the drive and sense modes is realized by integrating a polysilicon heater inside the spring beams. © 2002 Elsevier Science B.V. All rights reserved.

Keywords: CMOS-MEMS; Out-of-plane microactuation; Capacitive sensing; Comb drive; Inertial sensors

1. Introduction

Interdigitated comb drives have been widely used for electrostatic actuation, capacitive position sensing and frequency tuning. They have become an integral part of many MEMS devices such as accelerometers [1], gyroscopes [2–4], and microscanners [5]. However, most of these devices utilize the lateral capacitance change between comb fingers. The use of the vertical capacitance change between comb fingers is limited by parasitic capacitance to the substrate in polysilicon processes and electrical isolation difficulties in bulk micromachining processes.

A *z*-axis comb-finger accelerometer with an unbalanced proof mass was demonstrated by using the dissolved-wafer process [6]. An out-of-plane comb drive for a scanning micromirror has been fabricated in a high-aspect-ratio Si process [7]. Other than conventional interdigitated, engaged comb fingers, this *z*-comb drive has movable fingers (rotors) totally above stationary fingers (stators). High speed and large deflection were achieved, but a special Si wafer-to-wafer bonding process is needed.

In this work, we propose a unique *z*-axis comb-finger actuation and sensing method based on the CMOS-MEMS micromachining process developed in [8]. Mechanical and thermal properties of microstructures from this process have been studied and characterized [9,10]. CMOS accelerometers and gyroscopes also have been demonstrated [11–14].

A significant advantage of the CMOS-MEMS process is that out-of-plane actuation and displacement-sensing can be easily realized [12,15]. Therefore, three-axis capacitive actuation and sensing can be integrated on a single chip using a single mechanical layer. In this paper, the post-CMOS micromachining process is described first. A special beam design is proposed to compensate lateral curling of the microstructures. The principle of the *z*-axis comb-finger actuation and displacement-sensing is then introduced, followed by its application in a *z*-axis accelerometer, an *x*–*y*–*z* microstage and a lateral-axis gyroscope. Design issues and experimental results of all three devices are presented. Experimental results on motion sensing and mode coupling in the lateral gyroscope are addressed. A method of thermomechanically tuning resonance frequency for mode matching is proposed and experimentally verified.

2. Post-CMOS micromachining

The micromachining process is a maskless, two-step, post-CMOS process in which the etching masks are provided by

* Corresponding author. Tel.: +1-412-268-6607; fax: +1-412-268-4595.
E-mail address: xie@ece.cmu.edu (H. Xie).

0924-4247/02/$ – see front matter © 2002 Elsevier Science B.V. All rights reserved.
PII: S0924-4247(01)00740-3

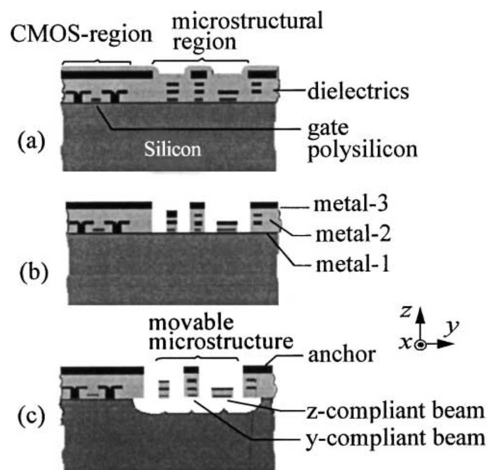

Fig. 1. Cross-sectional view of the thin-film CMOS-MEMS micromachining. (a) After standard CMOS processing; (b) anisotropic dielectric etch; (c) anisotropic and then isotropic silicon etch for release.

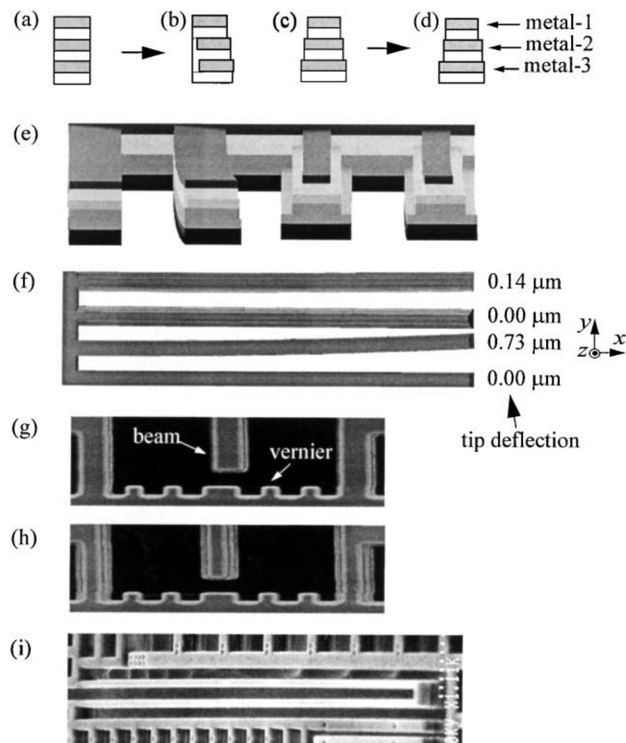

Fig. 2. Lateral curling elimination. (a) Normal beam; (b) normal beam with misalignment; (c) tapered beam; (d) tapered beam with misalignment; (e) side view of MEMCAD simulation result (the beams are 100 μm long; both vertical and lateral curling are visible); (f) top view showing lateral curling with 3X exaggeration of displacement, (g) SEM of a released normal beam, (h) SEM of a released tapered beam; (i) a tapered *y*-spring demonstrating near perfect lateral alignment.

the interconnect metal layers in the conventional CMOS process. Microstructures are made directly from the stack of CMOS interconnect layers. First, the microstructures are defined with an anisotropic reactive-ion-etch (RIE) of dielectrics in a CHF_3/O_2 plasma, as shown in Fig. 1(b). Second, a deep silicon RIE (DRIE) is performed by using the Bosch process [16], followed by an isotropic SF_6-plasma silicon undercut to release the microstructures, as shown in Fig. 1(c). The isotropic etch is achieved by greatly reducing the platen power. This process creates microstructures with high aspect-ratio and a high flexibility of wiring. The dry etch for release eliminates any sticking problems. The DRIE step provides independent control of the vertical gap to the substrate. The gap is chosen to be relatively large, which provides small squeeze-film damping of the out-of-plane modes and minimizes electrostatic coupling to the substrate. Curling from residual stress gradients in the composite films can be compensated to the first order via a curl matching frame [11]. All devices described in this paper were fabricated in the Hewlett-Packard 0.5 μm CMOS process followed by the post-CMOS micromachining.

The CMOS-MEMS process provides beams with different thicknesses by choosing different interconnect metal layers as etching mask. Typically, beams with metal-1, metal-2, metal-3 on the top are 1.8, 3.5, and 5.0 μm thick, respectively. Therefore, various flexible suspension beams (i. e. springs) can be designed (Fig. 1(c)). A vertically compliant spring (z-spring) is realized by using wide beams with metal-1 on the top, while a lateral-compliant spring is realized by using narrow beams with metal-3 on the top. For example, assuming a z-spring has a beam width of 10 μm. Since its beam thickness is 1.8 μm, the z-axis stiffness will be about 30 times smaller than the x-stiffness.

Another design issue with springs is the in-plane curling of spring beams, which results in lateral position offset [11]. This lateral curling is caused by the asymmetric cross-section of the spring beams that results from the process variations, especially from photolithography misalignment. For example, in Fig. 2(a), the three metal layers in the beam have identical width and are designed to be aligned. However, due to the finite precision of the photolithography, the metal layers will have certain misalignment. Since all metal layers can function as the structural etching mask, oxide will fill the vacancy left by any metal layer shift, as shown in Fig. 2(b). Lateral curling becomes worse as beam thickness decreases. In order to reduce this lateral curling, a special tapered beam is proposed. As shown in Fig. 2(c), lower level metal layers are made wider. As long as the width difference is larger than the photolithography error, there will be no oxide remaining beside any metal layer. Fig. 2(e) and (f) show the finite-element [17] simulation result in which the tapered beam has less than one-fifth of lateral curling as that of the normal beam even though the two beams are designed to have the same z-axis bending moment of inertia. The beams are 2.4 μm wide and 100 μm long. A misalignment of 0.1 μm between adjacent metal layers is considered. Fig. 2(g) and (h) are SEMs of two released beams with a normal design and a tapered design, respectively. The tapered beam significantly reduces the lateral curling.

3. Out-of-plane comb-finger actuation and sensing

As shown in Fig. 1, microstructures can have several embedded metal layers, which is a major difference from homogeneous polysilicon counterparts. These multiconductor layer structures make it possible to construct multiple capacitors between comb fingers. There are 22 different electrode-pair configurations for combs with three metal layers that provide vertical electrostatic actuation and capacitive displacement-sensing.

The cross-sections of two configurations of comb fingers are shown in Fig. 3(a) and (b). The comb fingers have two or three metal layers and are located about 25 μm above the substrate, which leaves ample room for vertical motion. This large gap is also an advantage for capacitive comb-finger sensing because the parasitic capacitance to the substrate is greatly reduced. As shown in Fig. 3(a), if the three metal layers on the stators are electrically connected, as are the corresponding metal layers in the rotor, the CMOS comb drive functions equivalently to a lateral-axis polysilicon comb drive.

If all three metal layers in the rotor are electrically connected while the metal-1 and metal-3 in the stator are separately connected, two sidewall capacitors, C_1 and C_2, are formed, as shown in Fig. 3(b).

When a voltage is applied across C_1 or C_2, the rotor will actuate in the z-direction. If the rotor finger moves up or down by an external force (such as acceleration), C_1 and C_2

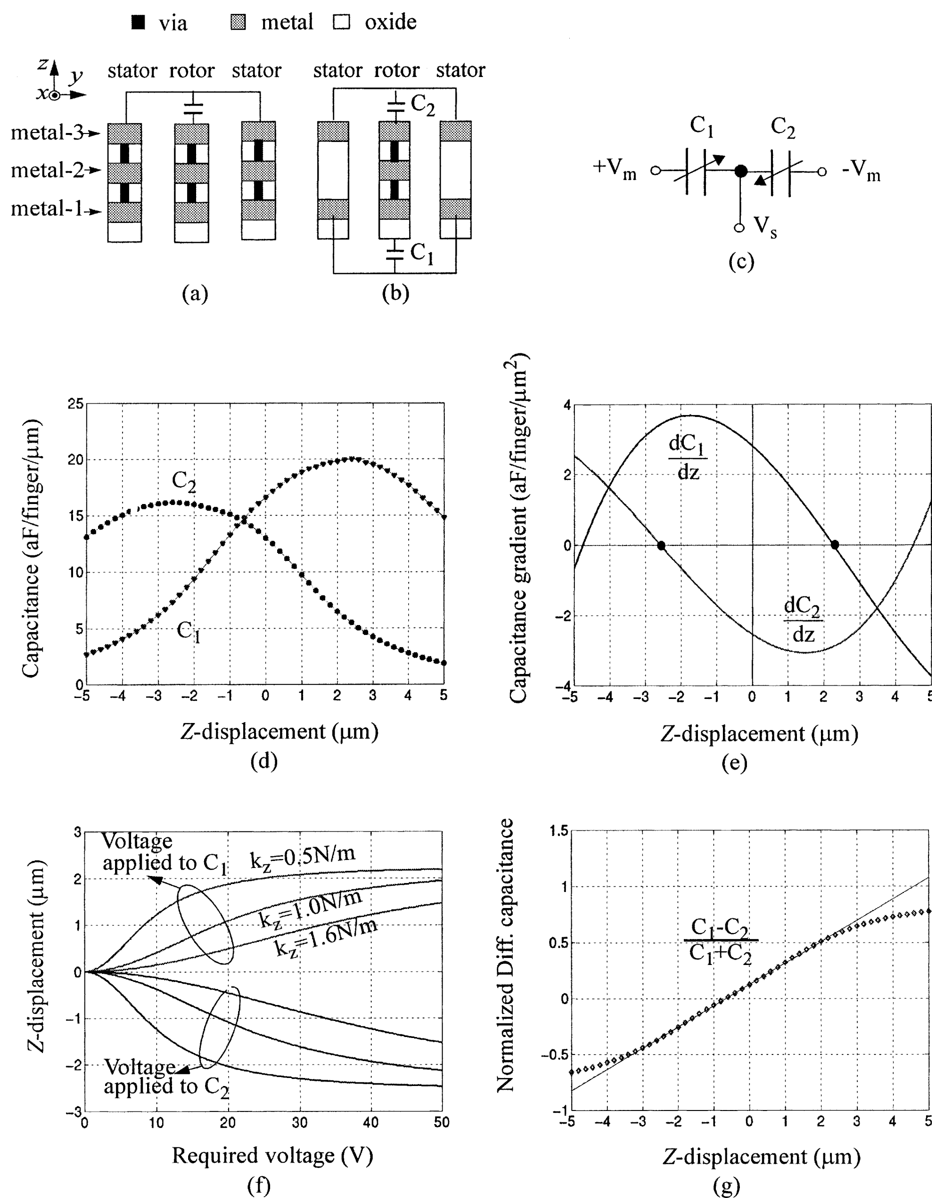

Fig. 3. Principle of vertical actuation and capacitive sensing through comb fingers. (a) x-Axis actuator; (b) z-axis actuator; (c) equivalent capacitive bridge; (d) capacitance vs. Z-displacement; (e) capacitance gradient vs. Z-displacement; (f) Z-displacement vs. applied voltage where fifty-two 30 μm long comb fingers are assumed; (g) calculated differential capacitance vs. Z-displacement.

will change value in opposite directions and therefore, the device can function as a z-axis motion detector.

3.1. z-Axis actuation

In order to evaluate the capacitance and expected displacement, a commercial finite-element analysis tool, the Maxwell two-dimensional field simulator [18], is employed. The calculated C_1 and C_2 in Fig. 3(b) and their gradients versus static Z-displacements are shown in Fig. 3(c) and (d), respectively. Note that the maximum displacement range is defined by the intersections of the two gradient curves with the zero-gradient line, which occur at −2.6 and 2.2 μm, respectively (Fig. 3(d)). The electrostatic force F_e is equal to

$$F_e = \frac{1}{2} NL \frac{dC}{dZ} V^2 \quad (1)$$

where N is the number of comb fingers, L the engaged length of comb fingers, and V the applied voltage. The relationship between displacements and required voltages can be obtained by numerically solving the force balance equation, i.e. $F_e = F_{spring} = kZ$, where k is the spring constant and Z is the vertical displacement. The result is plotted in Fig. 3(e) for a series of spring constants. Displacement tends to saturate at −2.6 and 2.2 μm when the voltage increases.

3.2. z-Axis displacement sensing

Capacitance change is often used as a measure of displacement in microaccelerometers. The sensitivity in one direction depends on both the capacitance gradient and the mechanical stiffness in that direction. As an electrical circuit, C_1 and C_2 form a differential capacitive half-bridge, as shown in Fig. 3(f). If balanced modulation voltages $\pm V_m$ are applied, the output signal V_s is expressed as:

$$V_s = \frac{C_1 - C_2}{C_1 + C_2 + C_p} V_m \quad (2)$$

where C_p is the parasitic capacitance. Fig. 3(g) shows the simulation results of C_1, C_2 and their differential change with Z-displacement. Parasitic capacitance in the CMOS microstructures is very small and in this theoretical analysis is set to zero. Although C_1 and C_2 are not linear with Z-displacement, the normalized differential capacitance changes linearly from −3.0 to +2.3 μm. If the rotor fingers are attached to a proof mass and a spring, the output voltage is

$$V_s = \frac{ma}{k} V_m \frac{d}{dZ} G(Z) \quad (3)$$

where $G(Z) = (C_1 - C_2)/(C_1 + C_2 + C_p)$, m is the mass of the proof mass, k is the stiffness of the spring in the z-axis, a is the extemal acceleration in the vertical direction and V_m is the modulation voltage. The sensitivity V_s/V_m depends on the spring, proof mass and capacitive bridge, but is constant as long as the system is operating in its linear range.

Note that the wide linear displacement range (−3.0 to +2.3 μm) is remarkable, since large dynamic range can be achieved without compromising sensitivity or bandwidth. Low cross-sensitivity is expected in this configuration because C_1 and C_2 are the summation of the capacitances formed in both sides of the stator and the stiffness of the lateral axes is designed to be much bigger than that of the z-axis.

The differential capacitance curve in Fig. 3(g) is not symmetric, i.e. $G(Z) \neq 0$ at $Z = 0$. Instead, a dc offset of 0.6 μm exists. The dc offset can be compensated by a prescribed displacement of 0.6 μm realized by properly designing the curl matching frame or by integrating a polysilicon heater [10].

4. z-Axis comb-finger accelerometer

Fig. 4(a) shows the topology of the z-axis accelerometer consisting of a central proof mass, two symmetric z-spring beams and two sets of comb fingers. The multiconductor layer structure makes it easy to implement full-bridge

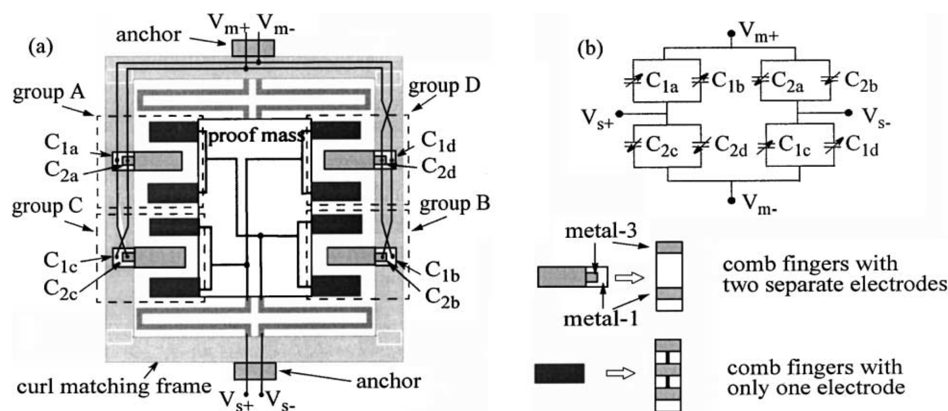

Fig. 4. Topology design and wiring configuration of the z-axis accelerometer. (a) Schematic of the top view of the layout with a common centroid configuration; (b) equivalent full-bridge differential capacitive interface.

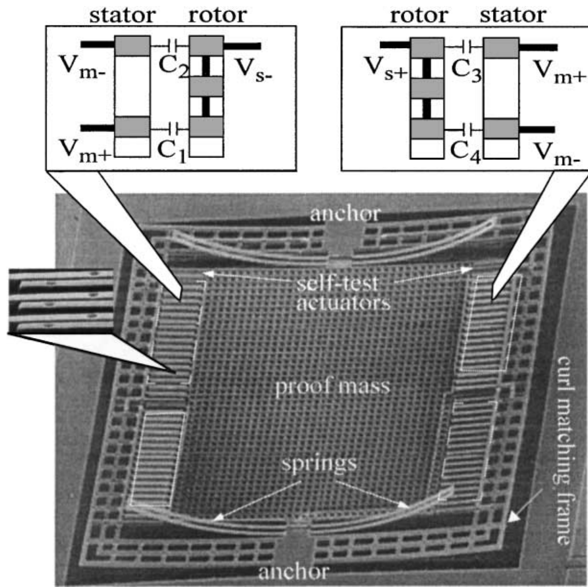

Fig. 5. Top view of a released z-axis accelerometer.

differential capacitive interfaces. The comb fingers are divided into four groups as shown in Fig. 4(a). All comb fingers have exactly the same cross-section as shown in Fig. 3(b). In groups A and B, the top metal layer is connected to V_{m+}, and the bottom metal layer to V_{m-}. In groups C and D, the wiring is reversed to obtain a full-bridge differential capacitive interface as shown in Fig. 4(b). Moreover, the four groups constitute a common centroid configuration which reduces the lateral-axis sensitivity and the influence of process variations.

A released accelerometer is shown in Fig. 5. The size of the device including the on-chip buffers and preamplifier is about 0.5 by 0.7 mm. The two sets of fingers outlined with a white solid line are electrically connected, as are the other two sets outlined with a white dashed line. Schematic cross-sections are shown at the top of the SEM. The spring beams curl up about 55 μm at their ends due to the residual stress gradients arising from the embedded layers inside the beams. However, the stator and rotor fingers align very well (<0.5 μm vertically and <0.1 μm laterally) through a curl matching frame. There is one extra pair of comb fingers at each corner of the proof mass. These comb fingers are electrically isolated from the sense comb fingers and are used as electrostatic actuators for self-test and offset adjustment.

The packaged accelerometer is mounted on a Brüel and Kjaer vibration exciter whose motion is monitored by a high accuracy reference accelerometer, and an HP4395A spectrum analyzer is used to measure the output signal. The measurement result in Fig. 6 is for a 200 Hz sinusoidal shaker excitation and an 800 mV 400 kHz sinusoidal modulation across the capacitive bridge. The output sensitivity is 0.5 mV/g. The response remains linear (<1% non-linearity) when the amplitude of the external acceleration increases to 27 g, which is the maximum limit of the shaker table. The

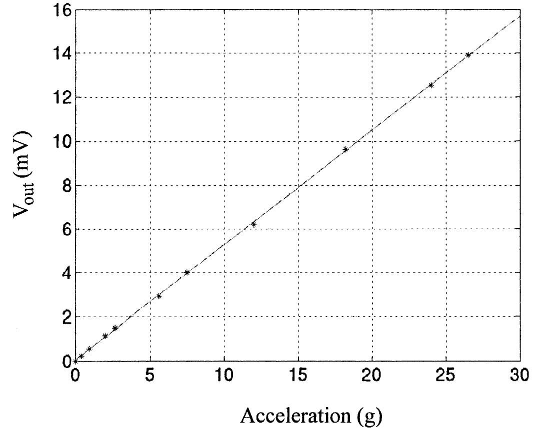

Fig. 6. Dynamic response of the accelerometer measured at 200 Hz using a shaker table.

theoretical linear range is ±600 g because of the wide linear range of the differential capacitance change with z-displacement. The measured noise floor is 6 mg/$\sqrt{}$Hz, which is one order of magnitude higher than the calculated Brownian noise. The increased noise level is believed to be due to the test circuits and vibration existing in the test environment.

The frequency response of the accelerometer is characterized by using a Michaelson optical interferometer system. Two microscope objectives are used to image the microstructure and a flat reference mirror simultaneously onto a CCD camera or a photodiode. These two interfering optical fields result in a fringe pattern that allows the evaluation of the topography and real-time displacement measurement. A He:Ne laser ($\lambda = 633$ nm) produces high intensity fringe patterns in the dynamic measurements, while a red LED ($\lambda = 610 \pm 10$ nm) is employed to avoid speckled images in the static measurements. LEDs also have the advantage of rapid pulsing capability.

A network analyzer sweeps the frequency of the actuator voltage to obtain the electromechanical transfer function.

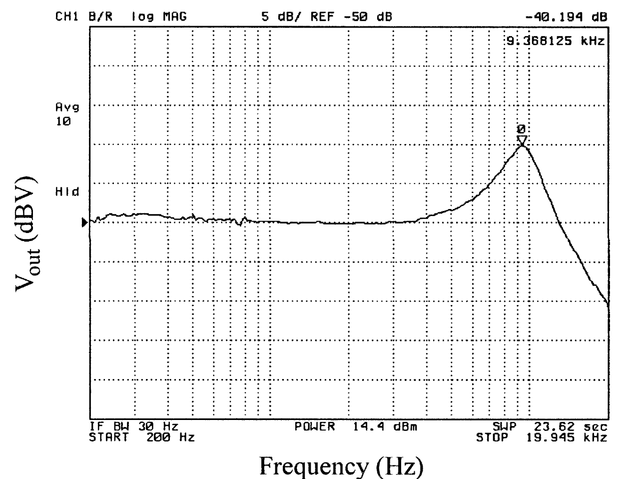

Fig. 7. Frequency response of the accelerometer measured by using the optical interferometer.

The output motion is measured using a photodetector that senses the fringe intensity at a spot on the proof mass. The measured frequency response is plotted in Fig. 7. The resonance frequency of 9.4 kHz is within 10% of the 10.1 kHz value predicted by finite-element analysis [17]. The difference is attributed to fabrication process variations and the simplification of modeling the perforated proof mass as a solid plate. The quality factor is about 3, resulting from the squeeze-damping of the proof mass.

5. *x–y–z* Microstage

Three-axis microstages have wide applications in micro-optics for precise adjustment of multi-axis scanning [19], optical switches and interferometer systems. The out-of-plane actuation is most challenging to implement within the CMOS-MEMS process.

The top view of the fabricated three-axis microstage is shown in Fig. 8. Separate sets of comb fingers for each direction drive the central proof mass. The *y*-axis and *z*-axis comb drives are suspended by a common set of springs that are flexible in both *y*-and *z*-directions. The device curls out of plane about 8 μm at the edges due to the residual stress gradient in the multilayer structures. However, as shown with the accelerometer, the stator and rotor fingers align well locally through use of a curl match frame.

The three-axis stage was operated in the *z*-axis to verify the vertical actuator model. The frequency response and displacement of the *z*-axis actuator were measured using the Michaelson interferometer system. The *z*-axis spring constant is 1.6 N/m. The experimental data does not fit exactly to the simulation in Fig. 3(f), because the released comb fingers have about 0.5 μm vertical mismatch and about

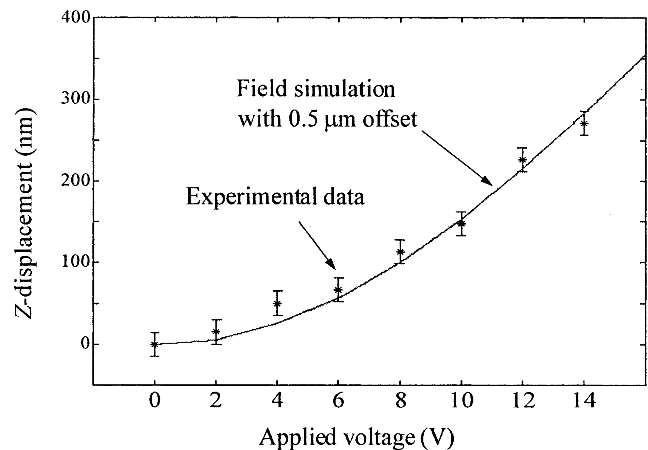

Fig. 9. *Z*-displacements vs. applied voltages.

0.1 μm sidewall overetch of metal-3. Fig. 9 shows the measured data and the field finite-element simulation result with the consideration of the mismatch and the metal-3 shrinkage. The experimental data fit the theoretical prediction well. Since the microstructure is not perfectly flat, the motions in *x*-and *y*-directions can also be detected through the interferometer measurements. The measured resonant frequencies in the *x*-, *y*-, and *z*-directions are 23.8, 5.08, and 6.17 kHz, respectively.

6. Lateral-axis gyroscope

Vibratory-rate gyroscopes sense Coriolis acceleration, which is proportional to the cross-product of velocity *v* of the vibrating structure and the external rotation rate Ω. These three parameters are orthogonal to each other, so a lateral-

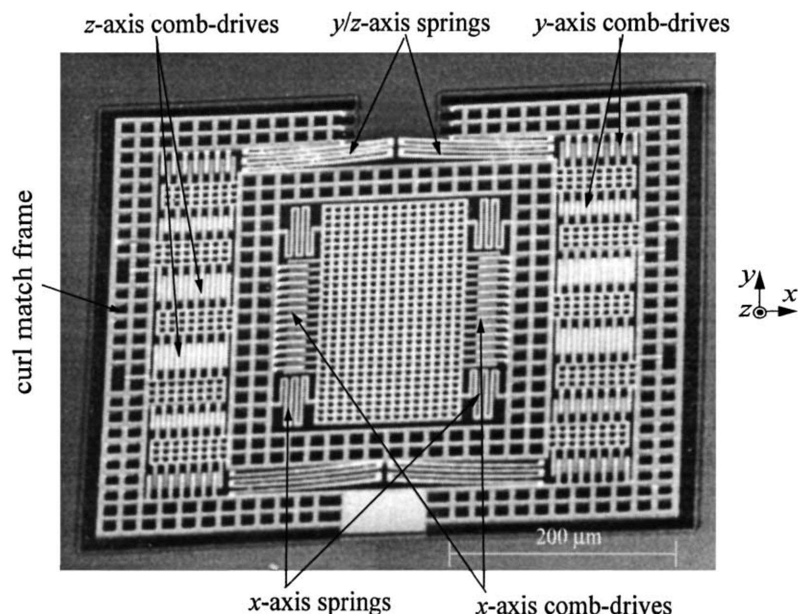

Fig. 8. SEM of *x–y–z* microstage.

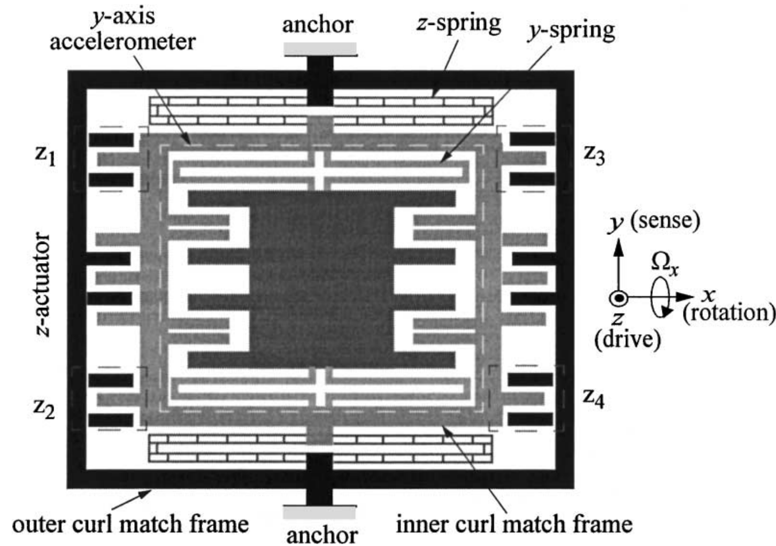

Fig. 10. Topology of the lateral-axis gyroscope.

axis microgyroscope needs either vertical actuation or vertical motion sensing. Considering the practical design issues with CMOS-MEMS, such as the mismatch between rotor and stator fingers and the requirement of curl matching frames, the *z*-axis actuation as described in the microstage is employed. In contrast, a vertical-axis CMOS-MEMS gyroscope has been implemented with no vertical actuation or sensing [13].

The topology of the lateral-axis gyroscope is shown in Fig. 10; which includes three key components: a *z*-axis comb drive, a *y*-axis accelerometer, and a *z*-axis position sensor used for feedback control of the *z*-axis actuation. The structure is a two-fold, orthogonal spring-mass system where the inner frame (together with the proof mass) is driven to vibrate in the *z*-direction by the comb drive while the induced Coriolis acceleration is sensed by the accelerometer. Thus, the rotation sense axis of this device is along the *x*-axis.

There are 180 comb fingers for *z*-axis actuation and 200 comb fingers for *y*-axis acceleration sensing. A *y*-axis actuator is also included inside the embedded *y*-axis accelerometer to compensate any off-axis motion coupled directly from the *z*-axis input excitation. Such coupling arises from manufacturing variations that cause imbalance in the proof mass and springs. Similar to the *z*-axis accelerometer, all the motion sensors in the gyroscope have four groups of comb fingers forming a common centroid configuration to reduce the influence of process variation.

Fig. 11 shows an SEM of a released gyroscope. The springs suspending the inner accelerometer are shown in

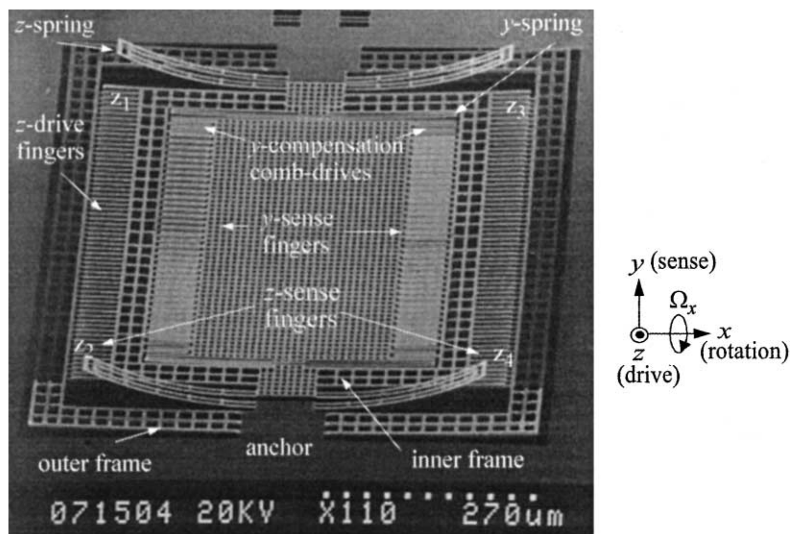

Fig. 11. SEM of a released gyroscope.

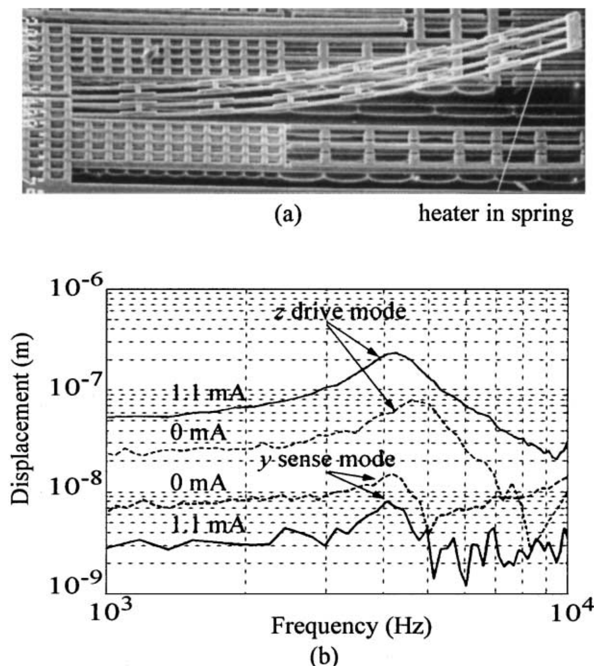

Fig. 12. Resonant frequency matching and mode coupling suppression through heating. (a) SEM of a z-spring beam with an embedded polysilicon heater; (b) frequency responses of the drive and sense modes with and without injecting current.

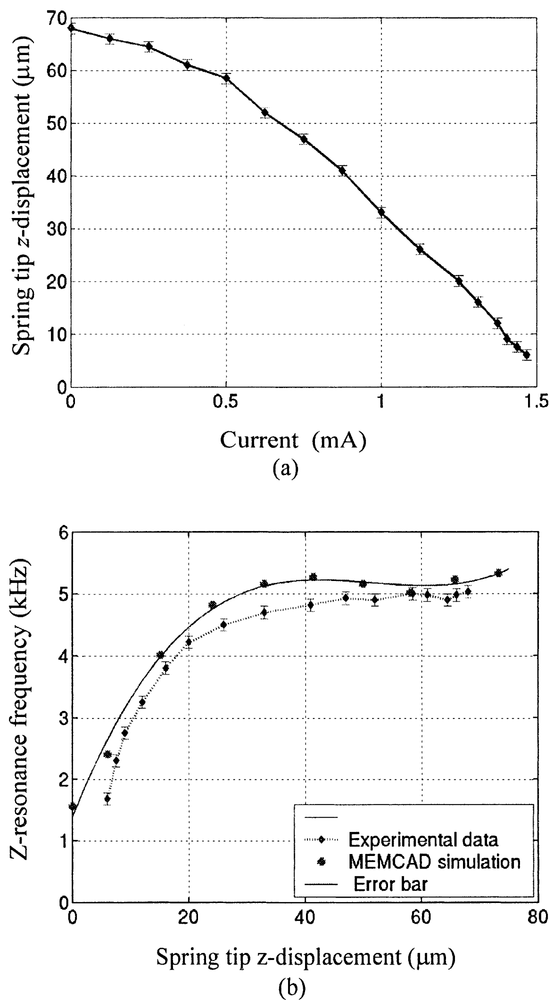

Fig. 13. (a) Thermomechanical curling compensation as a function of applied current; (b) resonant frequency tuning as a function of the Z-displacement at the cantilevered end of the spring.

Fig. 2(i) and exhibit minimal lateral curl. However, the ends of the beams on the z-axis suspension curl up 68 μm (Fig. 12(a)). This curling can be compensated by injecting a current through a polysilicon resistor inside the spring beams. With the aid of a MIT Microvison System [20], it was observed that flattening of the spring beams increases the suppression of the mode coupling and changes the resonant frequency of the drive mode (Fig. 12(b)). Meanwhile, the resonance of the sense mode stays almost unchanged. Therefore, the integrated heater provides an alternative method to match the resonant frequency between the sense and drive modes if necessary. The relationship between the heater current and the tip vertical deflection of the z-axis suspension beams is plotted in Fig. 13(a). Both the simulated and measured dependences of resonant frequency of the drive mode to the tip Z-deflection are shown in Fig. 13(b). A rapid change occurs when the spring beams approach the curl matching state at a heater current of 1.1 mA. The experimental result is in agreement with the finite-element prediction.

A fully-differential capacitive bridge is implemented, along with an on-chip differential preamplifier. A spectrum of the y-axis accelerometer response is plotted in Fig. 14 showing a resolution of 100 $\mu g/\sqrt{Hz}$. The gyroscope operated in air with no current injected into the polysilicon heater to flatten the z-axis springs. However, the coupled motion was large and drove the embedded y-axis accelerometer out of its linear range.

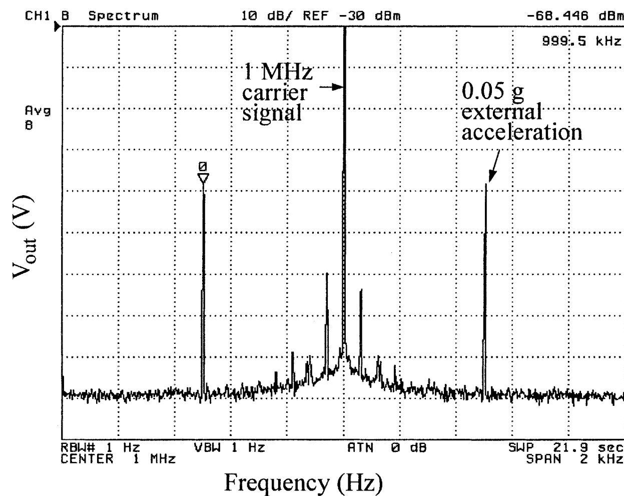

Fig. 14. Spectrum of the y-accelerometer at a 500 Hz, 0.05 g external acceleration, showing a resolution of 100 $\mu g/\sqrt{Hz}$.

7. Conclusions

Vertical comb-finger actuation and sensing for CMOS-MEMS is proposed and experimentally verified. Combining the inherent in-plane (lateral) actuation and sensing capacities of comb fingers, three-dimensional actuation and sensing can be realized. The demonstrated vertical actuation mechanism has been implemented in a three-axis microstage and a lateral-axis vibratory gyroscope.

The vertical actuation and sensing capability enables future design of three-axis accelerometers and full six degree-of-freedom inertial measurement systems on chip.

Based on the proposed method, the first design of CMOS-MEMS z-axis comb-finger accelerometers was successfully fabricated and characterized. The device has several advantages including low cost, large dynamic range, and on-chip integrated signal processing circuits.

A lateral-axis CMOS-MEMS gyroscope with vertical actuation is also demonstrated. The proposed thermal tuning by using an integrated polysilicon heater can be used to match the drive and sense modes, and can also be used for temperature compensation. It is experimentally verified that tapered beams significantly reduce lateral curling. However, this gyroscope design is not optimized. The drive spring and sense spring are in parallel because of the curl matching. This arrangement cannot obtain a high y-axis stiffness ratio between the two springs, resulting in low mode coupling rejection. In the next generation, the two springs will be orthogonal to each other. A key issue will then be how to achieve appropriate curl matching. Further gyroscope testing with coupled motion suppression by injecting current into the polysilicon heater and off-axis motion compensation by the integrated y-axis actuator is warranted.

Acknowledgements

The authors would like to thank Hao Luo, Xu Zhu, Suresh Santhanam and Dr. Lars Erdmann for circuit design, fabrication and measurement. This work was sponsored by DARPA under the AFRL, Air Force Materiel Command, USAF, under agreement F30602-97-2-0323.

References

[1] Accelerometer Product Family, Analog Devices Inc., Norwood, MA 02062, http://www.ana-log.com/imems.
[2] P. Greiff, B. Boxenhorn, T. King, L. Niles, Silicon monolithic micromechanical gyroscope, Technical Digest of the 1991 International Conference on Solid State Sensors and Actuators (Transducers 91), San Francisco, CA, USA, 24–27 June 1991, pp. 966–968.
[3] W.A. Clark, R.T. Rowe, R. Horowitz, Surface micromachined z-axis vibratory rate gyroscope, Technical Digest of the Solid-State Sensor and Actuator Workshop, Hilton Head Island, SC, USA, 3–6 June 1996, pp. 283–287.
[4] M. Lutz, W. Golderer, J. Gerstenmeier, J. Marek, B. Maihofer, S. Mahier, H. Munzel, U. Bischof, A precision yaw rate sensor in silicon micromachining, Technical Digest of the 1997 International Conference on Solid State Sensors and Actuators (Transducers 97), Chicago, IL, USA, 16–19 June 1997, pp. 847–850.
[5] M.-H. Kiang, O. Solgaard, K.Y. Lau, R.S. Muller, Electrostatic comb drive actuated micromirrors for laser-beam scanning and positioning, J. Microelectromech. Sys. 7 (1998) 27–37.
[6] A. Selvakumar, K. Najafi, A high-sensitivity z-axis capacitive silicon microaccelerometer with a torsional suspension, J. Microelectromech. Sys. 7 (1998) 192–200.
[7] R.A. Conant, J.T. Nee, K.Y. Lau, R.S. Muller, A flat high-frequency scanning micromirror, Technical Digest of the Solid-State Sensor and Actuator Workshop, Hilton Head Island, SC, USA, 4–8 June 2000, pp. 6–9.
[8] G.K. Fedder, S. Santhanam, M.L. Reed, S.C. Eagle, D.F. Guillou, M.S.-C. Lu, L.R. Carley, Laminated high-aspect-ratio microstructures in a conventional CMOS process, Sens. Actuators A 57 (1996) 103–110.
[9] M.S.-C. Lu, X. Zhu, G.K. Fedder, Mechanical property measurement of 0.5 μm CMOS microstructures, in: Proceedings of the Symposium on Microelectromechanical Structures for Materials Research, San Francisco, CA, USA, 1–16 April 1998, pp. 27–32.
[10] H. Lakdawala, G.K. Fedder, Analysis of temperature-dependent residual stress gradients in CMOS micromachined structures, Technical Digest of the 1999 International Conference on Solid-State Sensors and Actuators (Transducers 99), Sendai, Japan, 7–10 June 1999, pp. 526–529.
[11] G. Zhang, H. Xie, L. deRosset, G.K. Fedder, A lateral capacitive CMOS accelerometer with structural curl compensation, Technical Digest of the 12th IEEE International Conference on Microelectromechanical Systems (AJEM 99), Orlando, FL, USA, 17–21 January 1999, pp. 606–611.
[12] H. Xie, G.K. Fedder, A CMOS z-axis accelerometer with capacitive comb-finger sensing, Technical Digest of the 13th IEEE International Conference on Microelectromechanical Systems (MEMS 2000), Miyazaki, Japan, 25–28 January 2000, pp. 496–501.
[13] H. Luo, O.K. Fedder, L.R. Carley, An elastically gimballed CMOS-MEMS gyroscope, in: Proceedings of the International Symposium on Smart Structure and Microsystems, 19–21 October 2000, Hongkong, China.
[14] H. Xie, G.K. Fedder, A CMOS-MEMS lateral-axis gyroscope, Technical Digest of the 14th IEEE International Conference on Microelectromechanical Systems (MEMS 2001), Interlaken, Switzerland, 21–25 January 2001, pp. 162–165.
[15] H. Xie, L. Erdmann, Q. Jing, G.K. Fedder, Simulation and Characterization of CMOS z-axis Microactuator with Electrostatic Comb Drives, in: Proceedings of the 2000 International Conference on Modeling and Simulation of Microsystems (MSM 2000), San Diego, CA, USA, 27–29 March 2000, pp. 181–184.
[16] F. Laermer, A. Schilp of Robert Bosch OmbH, Method of Anisotropically Etching Silicon, US-Patent No. 5501893, 26 March 1996, filed 5 August 1994.
[17] MEMCAD User's Manual, Coventor Inc., Cary, NC 27513, http: //www.coventor.com.
[18] Maxwell 2D, Version 1.9.04, Copyright 1984–1997, Ansoff Corporation, Pittsburgh, PA 15219, http: //www.ansofi.com.
[19] L.Y. Lin, J.L. Shen, S.S. Lee, W.C. Wu, Surface-micromachined micro-X–Y–Z stages for free-space microoptical bench, IEEE Photon. Technol. Lett. 9 (1997) 345–347.
[20] W. Hemmert, M.S. Mermeistein, D.M. Freeman, Nanometer resolution of 3-D motions using video interference microscopy, Technical Digest of the 12th IEEE International Conference on Microelectromechanical Systems (M MS'99), Orlando, FL, USA, 17–21 January 1999, pp. 302–308.

Biographies

Huikai Xie received his BS and MS degrees in electronic engineering from Beijing Institute of Technology in 1989 and 1992, respectively. He obtained his second MSEE degree in electro-optics from Tufts University

in 1998. He currently is a PhD student in the Department of Electrical and Computer Engineering at Carnegie Mellon University. He was a research engineer in the Institute of Microelectronics at Tsinghua University working on various silicon-based chemical and mechanical sensors for 4 years. His present research interests include integrated inertial sensors, microoptics, microfabrication technologies and microelectromechanical multidomain simulation.

Gary K. Fedder is an associate professor at Carnegie Mellon University, holding a joint appointment with the Department of Electrical and Computer Engineering and The Robotics Institute. He received his BS and MS in electrical engineering and computer science from MIT in 1982 and 1984, respectively, and the PhD degree in electrical engineering and computer science from U.C. Berkeley in 1994. From 1984 to 1989, he worked at Hewlett–Packard on circuit design and printed circuit modeling. His present research interests include microsensor and microactuator design and modeling, integrated microelectromechanical systems manufactured in CMOS processes, and structured design methodologies for microelectromechanical systems.